

PLX: FLASH, OSIRIS, and HELIOS

Exploring the Physics of the Plasma Liner Experiment: A Multi-dimensional Study with FLASH, OSIRIS, and HELIOS

E. C. Hansen,¹ P. Farmakis,¹ D. Michta,¹ C. Ren,¹ H. Wen,¹ S. Langendorf,² F. Chu,²
and P. Tzeferacos¹

¹*University of Rochester, Rochester, New York 14627,*
USA

²*Los Alamos National Laboratory, Los Alamos, New Mexico 87545,*
USA

(Dated: 14 August 2025)

The Plasma Liner Experiment (PLX) at Los Alamos National Laboratory (LANL) is a platform that seeks to achieve fusion via a concept known as Plasma-Jet-Driven Magneto-Inertial Fusion (PJMIF). The experiment consists of three main phases: (1) target formation in which up to four plasma guns shoot magnetized hydrogen or deuterium-tritium jets to form a quasi-spherical target, (2) liner formation in which a constellation of 36 guns fire high-atomic-number (e.g., xenon) jets to form a liner shell, and (3) target compression in which the formed liner implodes the pre-formed target. Each phase of the PLX probes different plasma regimes with different physics at play, thus we simulated each phase separately and with multiple codes. Here we highlight some of the 1D, 2D, and 3D simulation results of all three phases from the *FLASH*, *OSIRIS*, and *HELIOS* codes. Some of the key physical processes involved include shock dynamics, kinetic effects, anisotropic thermal conduction, resistive magnetic diffusion, radiation transport, and magnetized jet dynamics. Our simulations show that the PLX can form a preheated (~ 40 eV), magnetized (electron Hall parameter > 1) target plasma, and a quasi-collisional liner shell that can subsequently compress the target to fusion-relevant conditions (e.g., temperatures > 1 keV).

I. INTRODUCTION

The pursuit of practical fusion energy remains a grand scientific and engineering challenge, with several promising approaches under active investigation^{1–4}. Among them, Plasma-Jet-Driven Magneto-Inertial Fusion (PJMIF) represents a hybrid method that seeks to combine the advantages of both magnetic and inertial confinement fusion^{5,6}. This novel concept employs high-velocity plasma jets to form a spherically symmetric liner, which compresses a magnetized fuel target to fusion conditions. The PJMIF approach has the potential to achieve high energy gain at relatively low driver energies, making it an attractive alternative to conventional fusion concepts.

The Plasma Liner Experiment (PLX) at Los Alamos National Laboratory (LANL) serves as a critical testbed for investigating the feasibility of PJMIF^{7–9}. The heavy, fast-moving plasma liner used to drive the implosion of the plasma target is formed from the merging and spherical convergence of an array of 36 supersonic plasma jets traveling at ~ 50 km/s¹⁰. Recent advancements have improved our understanding of PLX processes such as liner uniformity and jet merging dynamics and have guided the development of optimized jet configurations and injection parameters to enhance liner performance^{9,11}. A compatible magnetized plasma target that takes advantage of the high implosion speed of a spherically imploding plasma liner is injected into the vessel by merging 4~6 magnetized plasma jets with a magnetic field strength of ~ 1000 G at the gun nozzles. The collision of these plasma jets is expected to induce turbulence in the plasma target, resulting in tangled fields, which can provide very long connection lengths between the core and the liner surface thereby reducing thermal conduction losses from the fuel plasma to the colder liner^{12–14}. A comprehensive investigation into plasma target formation on PLX is scheduled to commence in late 2025.

The conditions in PJMIF implosions span a wide range of plasma parameter space and physical regimes, ranging from kinetic to fluid collisionality, optically thin to thick radiation transport, and weak to moderate magnetization. Some of the important physical processes include cold, high velocity jets merging at oblique angles during liner formation, target formation of a pre-heated magnetized plasma, anisotropic magnetized thermal conduction, and ultimately fusion thermonuclear burn and charged particle transport¹⁵. Due to the wide range of relevant physics, previous studies in PJMIF have often employed analytical or semi-

analytical approaches to predict performance.^{16,17} Integrated simulation efforts have been attempted and have addressed many first-order questions^{18–22}, but have often been limited in the breadth of the included physical effects. In this work, an attempt is made to rigorously simulate as many aspects of the concept as feasible with leading modern computational capabilities, and give improved insight into the detailed performance of PJMIF conceptual designs.

The structure of the paper is as follows: in Section II we describe the three codes used in this work: *FLASH*, *OSIRIS* and *HELIOS*. Then the paper is divided by the three phases of PLX: target formation (Section III), liner formation (Section IV), and target compression (Section V). Lastly, we summarize our conclusions in Section VI.

II. NUMERICAL METHODS

For the radiation-MHD modeling of the various stages of the PLX platform we employ the *FLASH* code²³. *FLASH* is a publicly-available, parallel, multi-physics, adaptive mesh refinement (AMR), finite-volume Eulerian hydrodynamics and MHD code, developed at the University of Rochester by the Flash Center for Computational Science (for more information on the *FLASH* code, visit: <https://flash.rochester.edu>). *FLASH* scales well to over 100,000 processors in modern high-performance computing architectures, and uses a variety of parallelization techniques like domain decomposition, mesh replication, and threading, to optimally utilize hardware resources. The *FLASH* code has a world-wide user base of more than 4,600 scientists, and more than 1,300 papers have been published using the code to model problems in plasma astrophysics, combustion, computational fluid dynamics, high energy density physics (HEDP), and fusion energy research.

Over the past decade and under the auspices of the U.S. Department of Energy (DOE) National Nuclear Security Administration (NNSA), the Flash Center has added in *FLASH* extensive HEDP and extended-MHD capabilities²⁴ that make it an ideal tool for the multi-physics modeling of the PLX platform. These include state-of-the art hydrodynamic and MHD shock-capturing solvers,²⁵ extended to a three-temperature formalism,²⁴ anisotropic thermal conduction that utilizes high-fidelity magnetized heat transport coefficients,²⁶ electron-ion heat exchange, multi-group radiation diffusion⁴, tabulated multi-material equations of state (EOS) and opacities, and numerous synthetic diagnostics²⁷. *FLASH*'s newest

algorithmic developments also include a complete generalized Ohm’s law that incorporates all extended MHD terms of the Braginskii formulation.²⁸ The new extended MHD capabilities are integrated with state-of-the-art transport coefficients,²⁹ developed with support from the U.S. DOE Advanced Research Projects Agency–Energy (ARPA-E) BETHE program. The *FLASH* code and its capabilities for magnetized HEDP have been verified through several benchmarks and code-to-code comparisons,^{30–33} as well as through direct application to numerous plasma physics experiments,^{34–42} leading to innovative science and publications in high-impact journals.

For the kinetic modeling of target and liner plasma jet merging processes we employ the *OSIRIS* code.^{43,44} *OSIRIS* is a state-of-the-art, fully explicit, multi-dimensional (1D, 2D slab and r - z , and 3D), fully parallelized, fully relativistic, particle-in-cell (PIC) code. *OSIRIS* is jointly developed by Instituto Superior Técnico Lisboa and University of California, Los Angeles (for more information on the *OSIRIS* code, visit: <https://osiris-code.github.io>). *OSIRIS* is highly optimized on a single core, and it scales well to over 1.5 million cores on the Sequoia supercomputer at Lawrence Livermore National Laboratory, maintaining 97% and 78% efficiency on weak and strong scaling, respectively. It has been run on many of the DOE and NSF leadership class computing facilities for over 15 years. On Blue Waters it has achieved 2.2 Pflops on a full-machine benchmark using more than 10 trillion particles. The *OSIRIS* code is used world-wide by more than 25 user groups to model problems in laser-plasma interaction, wake field acceleration, ion acceleration, plasma astrophysics such as shock formation, and fusion energy research.

OSIRIS includes higher order particle shapes, which limits self-heating effects related to aliasing, and includes energy and momentum conserving algorithms. The parallelization is done either using domain decomposition with MPI only or by using a hybrid approach where MPI is used across nodes and OpenMP parallelization is used within a node; both approaches support dynamic load balancing at the MPI level.⁴⁵ The dynamic load balancing feature can greatly speed up the plasma jet collision simulations because the computation time for each time step is roughly proportional to the number of particles inside the MPI nodes. The spatial distribution of the number of particles changes drastically as the simulations progress. There is a relativistic two-body Coulomb collision model^{46–48} as well as a hybrid algorithm⁴⁹ which pushes particles throughout all regions, but in a high-density region (collisional), MHD field equations are used to solve for the fields. This is useful in simulations of plasmas

with a large density range where some parts of the system are collisionless while others are collisional.

Results are also compared with *HELIOS*, a lightweight 1D Lagrangian fluid code that includes physics packages useful for HEDP such as tabulated EOS, flux-limited radiation diffusion, and thermal conduction.⁵⁰ Of particular interest in this study, the 1D Lagrangian formulation will exactly preserve a material interface (between liner and target) with no numerical diffusion or mixing between the two species. In a realistic case, mixing may occur due to various physical mechanisms including Rayleigh-Taylor instabilities, but the comparison of the 1D Lagrangian-to-Eulerian codes allows a convenient way to gauge the pure numerical diffusion that may be occurring in the Eulerian codes as a function of grid resolution, separate from physical mechanisms.

III. TARGET FORMATION

We ran a 2D axisymmetric *FLASH* simulation of two counter-propagating jets to demonstrate how a target plasma is formed from the jet collision. The code solves the three-temperature resistive MHD equations with anisotropic thermal conduction, electron-ion heat exchange, and multi-group radiation (six groups). For the jets, we used newer thermal conductivity²⁶ and magnetic resistivity²⁹ coefficients, and *PROPACEOS* tables for multi-group opacities. The domain extends axially from 137 cm to -137 cm (the diameter of the PLX chamber), and spans 68.5 cm radially. We used adaptive mesh refinement to achieve a maximum effective resolution of nearly 32 cells across the initial outer jet radius.

The jets are modeled as fully-ionized hydrogen with an ideal EOS ($\gamma = 5/3$). They are initialized with an inner radius of 1.5 cm (the plasma gun wire radius) and an outer radius of 4.25 cm. Between these radii, the jets are given a mass density of 2×10^{-8} g/cm³, a velocity of 80 km/s, electron and ion temperatures of 1 eV, and a radiation temperature of 0.1 eV. These parameters are enforced as inflow conditions at the lower and upper z domain boundaries, which are also treated as solid reflecting walls from $r = 0$ to 1.5 cm and beyond 4.25 cm. The solid wall regions of the domain boundaries do not allow any hydrodynamic motion, but they will allow thermal, radiation, and magnetic diffusion to pass through them. A radially-varying azimuthal magnetic field is imposed for the entire radial extent at these boundaries: it has a peak value of 2500 G at 1.5 cm with a linear profile from $r = 0$ cm to 1.5

cm, a $1/r$ profile from 1.5 cm to 4.25 cm, and a value of zero beyond 4.25 cm. This magnetic field profile is also imposed every time step in the first row of cells inside the domain; this helps reduce the imbalance of hydromagnetic pressure with the inflow conditions for better control of the jet velocity.

Since *FLASH* cannot simulate a true vacuum, the PLX chamber or ambient region is initialized with a low density of 2×10^{-11} g/cm³, and with thermal conduction and radiation absorption and emission turned off. The electron and ion temperatures are initialized to 1 eV and radiation temperature to 0.1 eV everywhere inside the domain. The difference in density between the vacuum and jet material creates a pressure imbalance which increases the forward jet velocity and also causes the jets to expand radially into the vacuum. There are also $\mathbf{J} \times \mathbf{B}$ forces from the azimuthal magnetic field that pinch the jet towards $r = 0$ during its propagation. Once the pinched jet material reaches the symmetry axis, it has no choice but to move axially, which leads to a streamlining of the jet head, observed as an overall acceleration of the jet; this is a well-documented phenomenon sometimes referred to as the nose-cone effect (see Hansen *et al.*⁵¹ and references therein). The combined effects of the enforced jet inflow velocity, pressure imbalance, and $\mathbf{J} \times \mathbf{B}$ pinch forces result in an average jet velocity (from $t = 0$ s to collision) of about 125 km/s, which is higher than the reported experimental values⁵² but not necessarily inconsistent. Previous experiments measured the jet velocities at positions near the gun and slightly downstream and reported a possible range of 30-100 km/s. Given the aforementioned acceleration mechanisms, an average value of 125 km/s over the entire axial extent is plausible.

Fig. 1 shows a density and electron temperature map of the jets after they have collided and formed a target plasma. Note that some amount of jet material is left behind or expands outwards away from the target-forming region. This effect can be mitigated by adding more jets; the experimental platform currently employs four target-forming jets, but may use more in the future. Also, some of the jet material will be swept up by the liner-forming jets during the subsequent liner-forming process. As the jets collide, material is forced outwards radially created an elongated pancake-like target. This effect can also be mitigated by adding more jets to the process, which would result in a more spherical target. In the end, the target reaches a volume-averaged density of approximately 1.67×10^{-10} g cm⁻³.

The temperature map of Fig. 1 shows that the hottest plasma forms a shell around the newly formed target. These outermost regions of the target plasma are similar to accretion

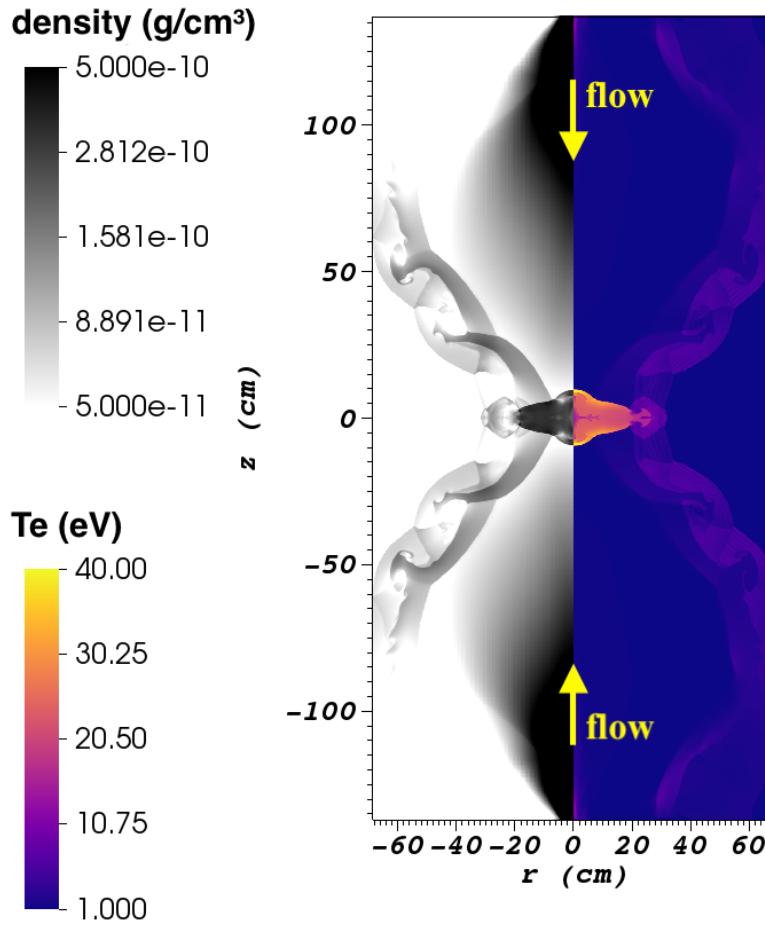


FIG. 1. Mass density (g cm^{-3}) and electron temperature (eV) of two colliding jets that have formed a target plasma from a 2D axisymmetric *FLASH* simulation. This target reaches a volume-averaged density of $1.67 \times 10^{-10} \text{ g cm}^{-3}$ and peak preheat temperatures of around 40 eV.

shocks where jet material is piling up and ramming into the expanding target. Since the magnetic field is azimuthal and the hot shell has a relatively lower magnetic resistivity, the magnetic field has increased difficulty leaving the shell region. This in turn can assist in thermally insulating the target via reduced thermal conductivity, which is included in the anisotropic thermal conduction implementation in *FLASH*. Some amount of preheat before the incoming liner compresses the target is crucial to the overall process, and we observe peak temperatures of around 40 eV in the jet collision simulation.

Our analysis included volume-averaging several quantities over a region about the center of the domain from $r = 0$ to $r = 25 \text{ cm}$ and $z = -15$ to $z = 15 \text{ cm}$. In this region, the

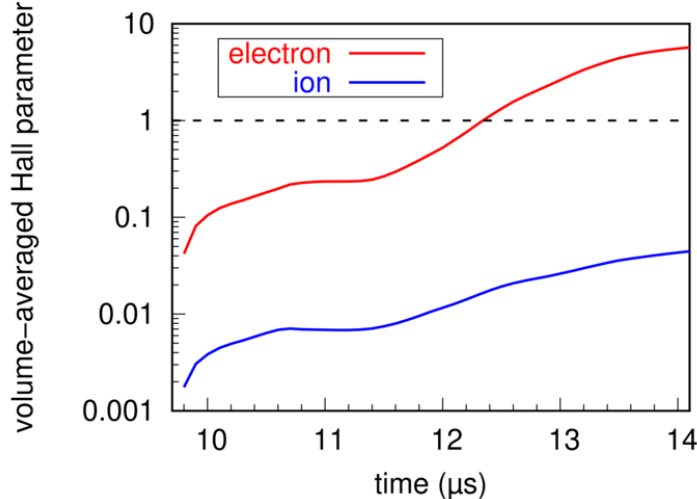


FIG. 2. Volume-averaged electron (red) and ion (blue) Hall parameters from the 2D jet collision simulation as a function of time. The values are averaged in a region where the target plasma is forming from $r = 0$ to $r = 25$ cm and $z = -15$ to $z = 15$ cm. Charged particles are considered magnetized when their Hall parameter is above 1.0 (denoted by the black dashed line), which eventually occurs, in this case, for electrons but not for ions.

target attains a volume-averaged number density of approximately $1 \times 10^{14} \text{ cm}^{-3}$, which would increase experimentally with more jets. We also expect the final volume-averaged magnetic field strength, 24.4 G, to increase with the number of jets. Fig. 2 shows the volume-averaged Hall parameters for electrons ($\langle \chi_e \rangle$) and for ions ($\langle \chi_i \rangle$) as a function of time. The target plasma reaches $\langle \chi_e \rangle > 5.0$, which is consistent with previous *FLASH* and *OSIRIS* simulations of target formation⁵³ that reported electron Hall parameters greater than unity. Also, the attained average plasma β (ratio of thermal pressure to magnetic pressure) was slightly greater than 100. This indicates that the magnetic field is strong enough to assist in thermally insulating the target plasma while not being dynamically significant, which is one of the primary goals of the PLX target formation process.

The results from this jet collision simulation are used to inform the initial conditions for 3D experimental-scale target compression simulations presented later in this work (Section VB).

IV. LINER FORMATION

In the full experimental-scale PLX, the liner shell is formed using 36 plasma guns, but some of the key physics can be studied by simulating the merging of just two jets. The primary goal of our liner formation simulations was to understand which conditions lead to fluid-like regimes (collisional) and which lead to more kinetic-like regimes (collisionless). This jet-merging process in the context of PJMIF was recently studied by Cagas *et al.*⁵⁴, and their results were consistent with some early findings from the PLX. Fluid codes (e.g., *FLASH*) will always produce shocks when the two jets collide, but these shocks can be mitigated through the collisionless interpenetration of the jets, a process that requires a kinetic model (i.e., not a fluid code). Here we have chosen to simulate the merging of two liner jets with both a kinetic code (*OSIRIS*) and a fluid code (*FLASH*) to make direct comparisons that help quantify the collisionality of the liner formation phase.

A. *OSIRIS* Simulations

A series of 1D *OSIRIS* simulations were conducted to quantify the interpenetration during the liner-liner jet merging process. A transition from a collisional to collisionless regime was observed as the initial jet velocity was increased. In these simulations, two singly-charged xenon plasma jets with density $n_{Xe} = 4.13 \times 10^{16} \text{ cm}^{-3}$ were initialized with equal electron and ion temperatures $T_e = T_{Xe} = 1.5 \text{ eV}$. The two jets counter-propagated with velocity v_j , where v_j is the controlled parameter. Fig. 3 shows the evolution of the plasma jet density, where the white lines correspond to the density profile of the left jet at the end of the simulation. At very high jet velocities (e.g., $v_j = 50 \text{ km/s}$), the merging of the two jets was collisionless; the left jet could fully interpenetrate through the right jet, as indicated by the white line in Fig. 3(a) (i.e., the final left jet density profile peaks on the right side of the domain). At very low jet velocities (e.g., $v_j = 13 \text{ km/s}$), the merging of the two jets was collisional; the left jet was mostly stopped by the right jet with minimal interpenetration as shown in Fig. 3(d). At intermediate velocities, the two jets can partially interpenetrate and form a broad density profile that peaks near the center, which is desirable for the PLX design. These results are consistent with the theoretical estimates of the ion mean free path, which is close to the liner jet size (5 cm) at $v_j = 27 \text{ km/s}$.

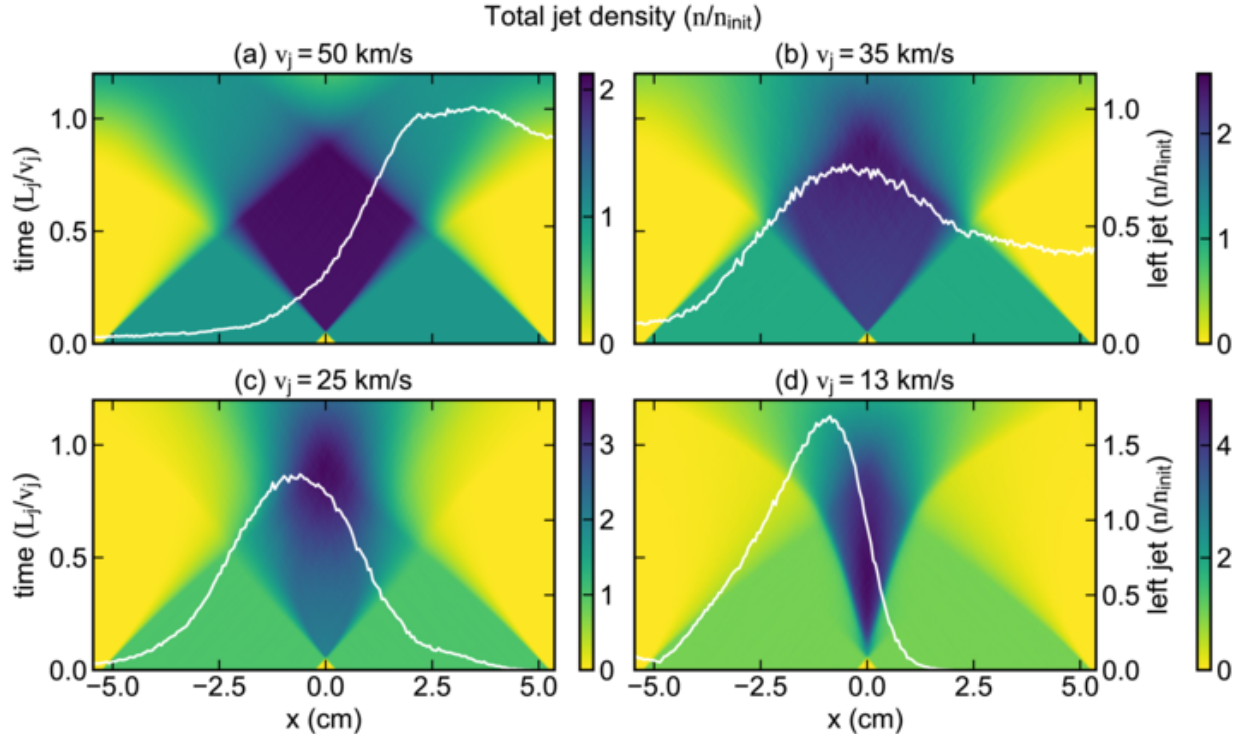


FIG. 3. Density evolution of two Xe liner plasma jets modeled using 1D *OSIRIS*. The horizontal axis is position (cm), left vertical axis is time in units of jet crossing times, and the total density (normalized to the initial value) is represented by the color map. The white lines represent the density profile of the left jet at the end of the simulation, normalized to the initial value and plotted with the right vertical axis; the location of the peak indicates how much the jets have interpenetrated. More interpenetration was observed at higher jet velocities.

B. *FLASH* Simulations

In this section, 1D liner-liner jet merging simulations conducted with *FLASH* are presented and compared with those from *OSIRIS*. This comparison aims to better delineate the transition from collisional to collisionless regimes and to identify any additional hydrodynamic effects. The simulation setup for the two counter-propagating xenon jets is consistent with the previous subsection, aside from the introduction of a low-density pseudo-vacuum, with a density four orders of magnitude lower than the jet density. Both the jets and the pseudo-vacuum are modeled using an ideal gamma-law EOS, with $\gamma = 5/3$. Thermal conduction and electron-ion heat exchange are described with Spitzer models.⁵⁵

FLASH is able to simulate radiation transport using a multi-group diffusion model. The

opacities for the jets and the pseudo-vacuum were tabulated using the *PROPACEOS* code. The initial radiation temperature was set to be in equilibrium with the ions and electrons, at $T_{rad} = 1.5$ eV. Simulations were conducted both with and without the inclusion of radiation transport.

Fig. 4 shows the evolution of total density in simulations using *OSIRIS*, *FLASH* without radiation transport, and *FLASH* with radiation transport, at four different jet velocities. In the collisional regime, observed at lower jet velocities ($v_j = 13$ and 25 km/s), *FLASH* simulations without radiation transport show qualitative similarities with *OSIRIS*. However, the behavior diverges at higher velocities, with *OSIRIS* jets interpenetrating, while the *FLASH* jets compress to a higher density. Including radiation transport in *FLASH* modifies the dynamics, providing an additional energy reservoir for work done to compress the jets, leading to further collapse of the liner.

V. TARGET COMPRESSION

The final phase of the PLX is target compression, during which fusion-relevant conditions may be attained. We studied several aspects of the target compression process: kinetic effects of a heavy liner colliding with a lighter target plasma, how liner perturbations affect implosion dynamics, and the fusion-relevant performance of an idealized reactor-scale compression. In all of the simulations that follow, assumptions were made about a pre-formed target plasma and a pre-formed liner plasma shell to study target compression independently from the other PLX phases.

A. 1D Code-to-code Comparisons

The kinetic process of target compression was investigated with a 1D *OSIRIS* simulation in Cartesian geometry. The initial condition of the PIC simulation is illustrated in Figs. 5(a) and 5(b). A 5 cm singly-charged ($Z = 1$) xenon liner propagated from right to left with velocity $v_x = 50$ km/s and collided with a 20 cm stationary fully-ionized hydrogen fuel that was magnetized by a 50 T magnetic field. Reflecting boundary conditions were used for both fields and particles. The initial densities for the liner and fuel plasma were 4.1×10^{16} cm $^{-3}$ and 5.4×10^{16} cm $^{-3}$, respectively. The simulation grid size was on the same order

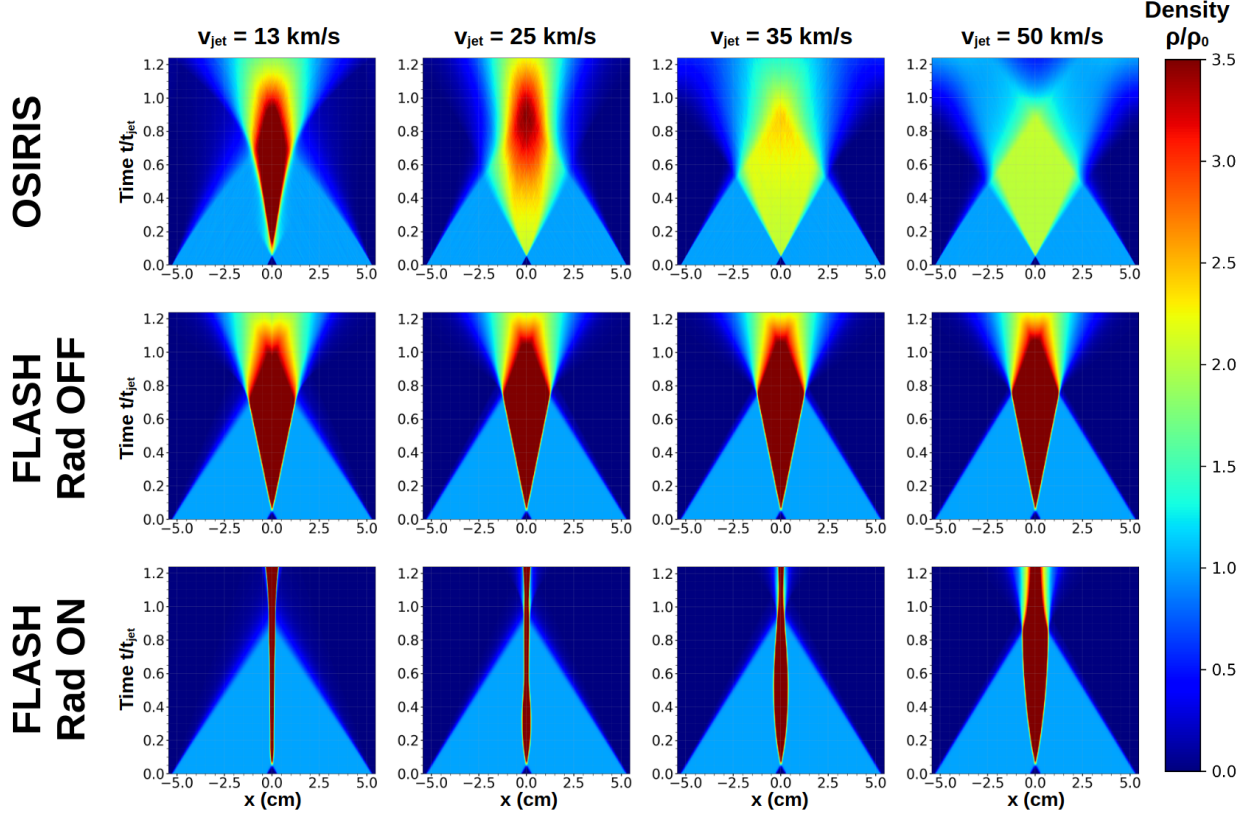


FIG. 4. Total density evolution in 1D liner jet merging simulations using *OSIRIS*, *FLASH* without radiation transport, and *FLASH* with radiation transport, for four jet velocities. *FLASH* simulations without radiation transport align with *OSIRIS* in the low-velocity (non-interpenetrating) regime. The inclusion of radiation transport in *FLASH* results in a more pronounced collapse of the liner.

as the Debye length of the fuel with temperature $T_{\text{fuel}} = 50$ eV, which consequently did not resolve the cold liner ($T_{\text{liner}} = 1.5$ eV). To reduce the numerical heating of the liner, a high-order current-smoothing and field-smoothing scheme⁵⁶ was used. The total energy increased by about 7% at the peak compression of the fuel, which is much less than the change in fuel thermal energy. At $t = 0$, the majority of the energy was stored in the form of the liner kinetic energy. During the liner-fuel compression process, the liner kinetic energy was converted into thermal energy of the liner and fuel. Both the liner and fuel plasma were heated as evidenced by the broadening of the phase spaces along the v_x axis shown in Figs. 5(c) and 5(d). As shown in Fig. 5(c), the magnetic field was also compressed by the liner, keeping the B/n_H ratio nearly constant within the fuel region.

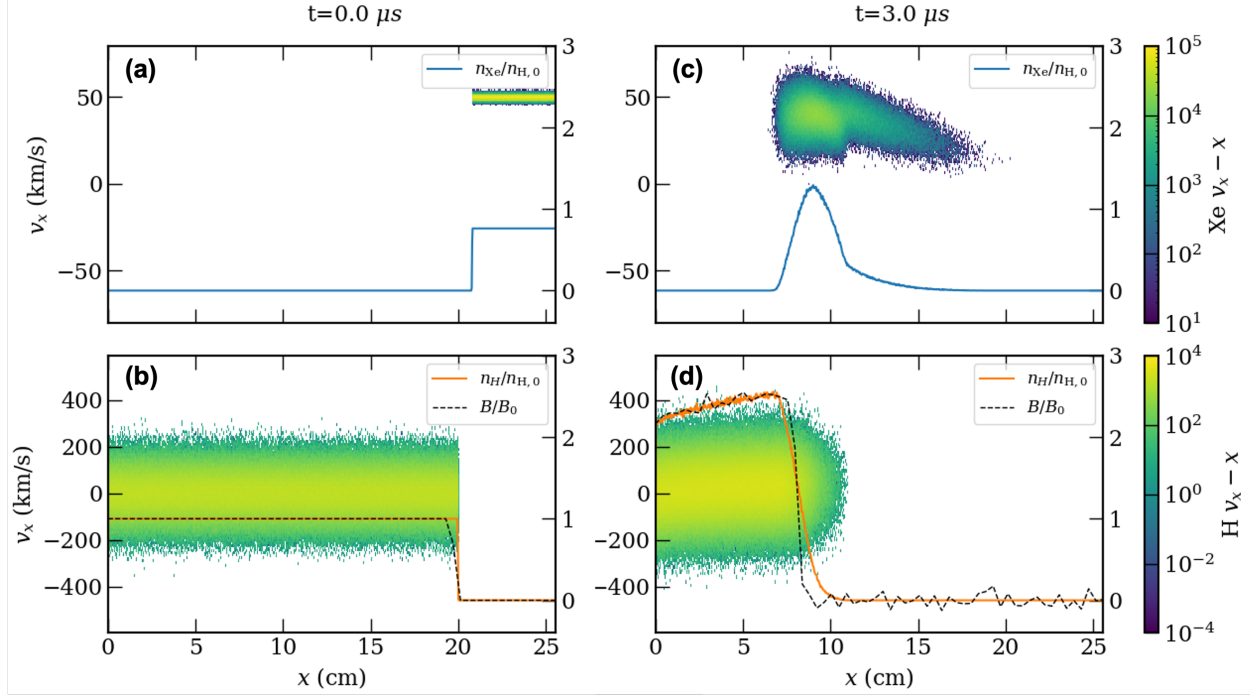


FIG. 5. The v_x - x phase space (plotted with left vertical axes) of the liner (upper row) and the fuel (bottom row) at $t = 0$ (left column) and $t = 3.7 \mu s$ (right column). The color bars represents particle number density in arbitrary units, to illustrate where in phase space the liner and fuel plasmas exist. The blue and orange solid lines correspond to the densities of the liner (n_{Xe}) and fuel (n_H) plasmas, respectively. The black dashed line corresponds to the amplitude of the external magnetic field (B). The densities were normalized to the initial value of the fuel, the external magnetic field was normalized to its initial value (50 T), and they are both plotted with the right vertical axes.

The evolution of the fuel density and temperature obtained from the PIC simulation agrees with the MHD simulations qualitatively as illustrated in Fig. 6. All three codes predicted peak compression to occur at about $t = 4.5 \mu s$. The maximum temperature and density achieved in the *OSIRIS* simulation were slightly lower than those achieved in the *FLASH* and *HELIOS* simulations, which is likely due to mixing of the liner and fuel plasmas. This mixing also resulted in a shallower density gradient as shown in Fig. 6.

In the *OSIRIS* simulation, a low-pass filter was applied to the electromagnetic field in the region $x > 18$ cm after $t = 3.8 \mu s$ to suppress a numerical instability observed in that region. Since the plasma density in that region is very low ($< 0.01 n_{H,0}$) after $t = 3.0 \mu s$,

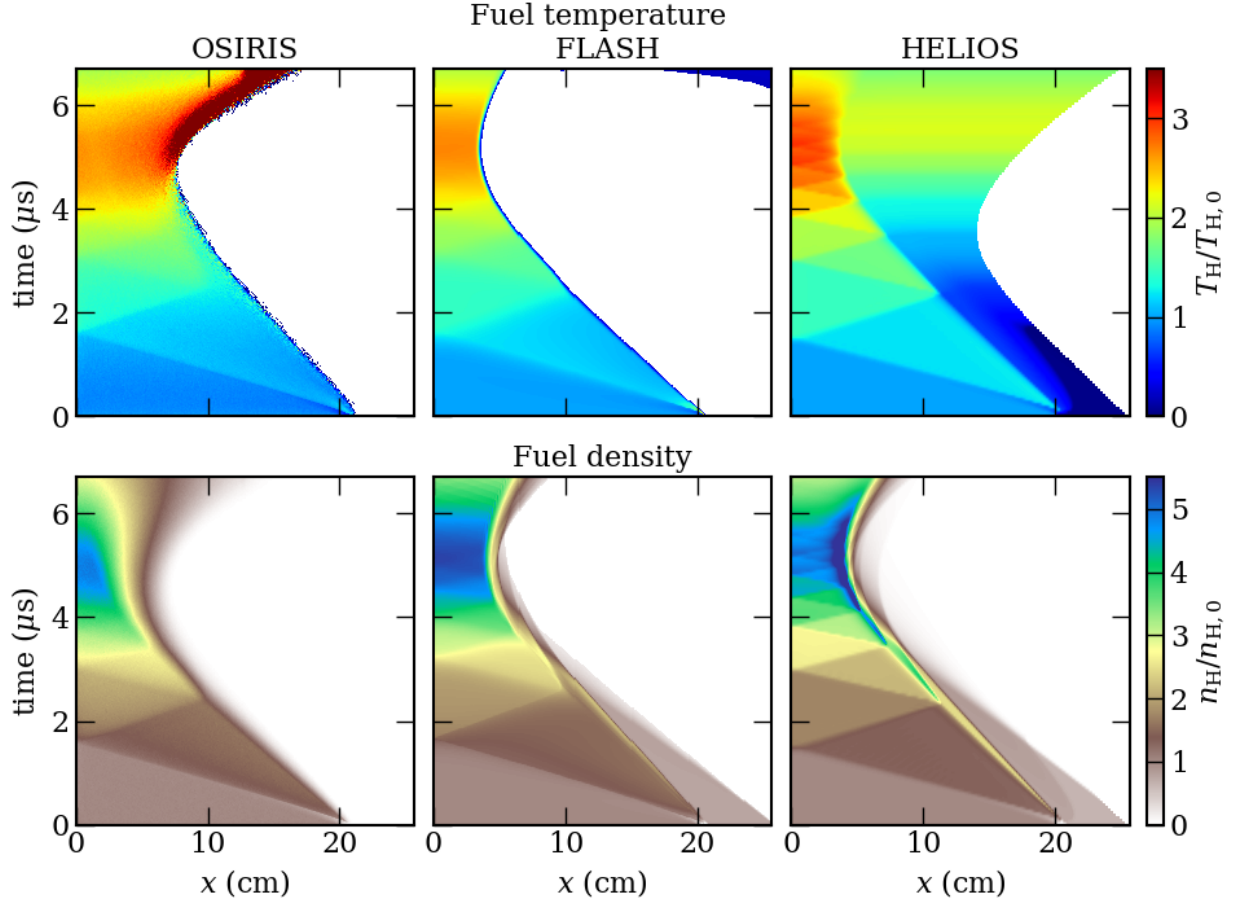


FIG. 6. The evolution of the temperature (upper row) and density (bottom row) of the fuel obtained from *OSIRIS* (left column), *FLASH* (middle column), and *HELIOS* (right column) simulations. All quantities are normalized to their respective initial values. All three codes yielded quantitatively consistent results.

we do not anticipate the additional low-pass filter to influence the physics of the liner-fuel compression which happened in the region $x < 10$ cm. Any meaningful influence should travel at the Alfvén speed from $x > 18$ cm to $x < 10$ cm, which would take more than $1 \mu\text{s}$. As shown in Fig. 6(a), the high temperature in the liner-fuel mixing region after the peak compression is likely an artifact due to an insufficient number of particles in that region.

Fig. 7 shows the evolution of the spatially resolved fuel concentration which is defined as $n_H/(n_H + n_{Xe})$. We observe evidence of mixing, which helps explain the slightly lower temperatures in the *OSIRIS* results.

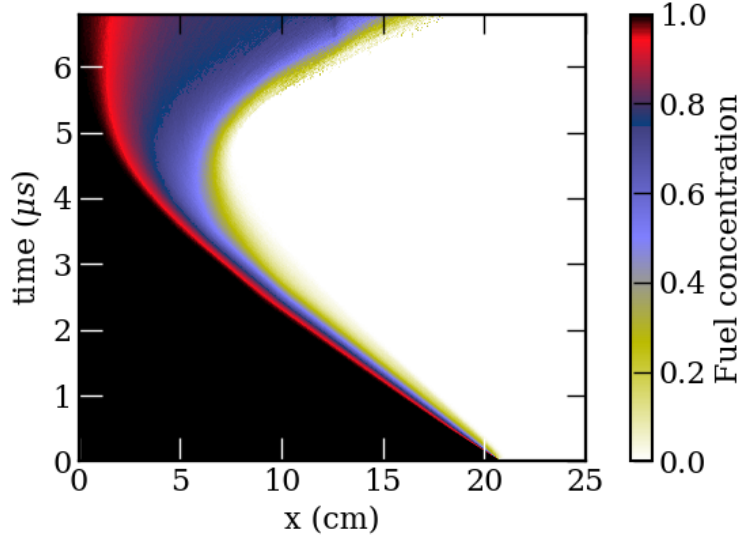


FIG. 7. The evolution of the spatially resolved fuel concentration ($n_H/(n_H + n_{Xe})$) obtained from the *OSIRIS* simulation. The fuel-liner mixing is limited in the central part of the fuel region.

B. 3D *FLASH* Simulations

High-resolution 3D simulations would have been too computationally expensive for *OSIRIS*, and *HELIOS* only operates in 1D. We must therefore turn to the *FLASH* code for high-fidelity 3D simulations of the target compression phase. Our first goal was to study the effects of liner perturbations on implosion dynamics, since the liner formation process is not likely to produce a perfectly homogeneous shell.

In all three simulations of this subsection, we used results from the 2D *FLASH* target formation simulation (see Section III) to inform the initial conditions of the target plasma. Since the previous jet collision simulation used two jets, it was reasonable to multiply the target density by a factor of two to approximate a target formed from four jets, which is the number of target-forming plasma guns employed by the current PLX design. Therefore, the hydrogen target was initialized with a density of approximately $3.35 \times 10^{-10} \text{ g cm}^{-3}$. The initial target temperature was set to 40 eV, a level of preheat observed in the target formation simulation. The target is assumed to initially be perfectly spherical with a radius of 25 cm, resolved with a minimum cell width of 0.125 cm.

Inside the target, we add pseudo-random perturbations ϵ to a constant vector potential \mathbf{A} , and then $\nabla \times (\mathbf{A} + \epsilon)$ gives the initial randomized magnetic field. Each component of \mathbf{A} uses a different pseudo-random number α_i , ranging from -1 to 1, for each computational

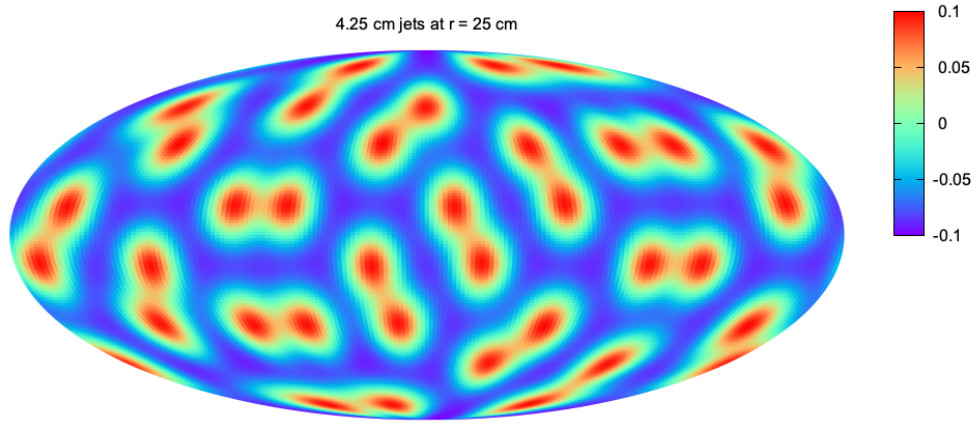


FIG. 8. A spherical slice of the mathematical form (i.e., dimensionless) of the liner perturbations taken at a radius of 25 cm (the inner liner radius) projected to a 2D map. Each spot on the surface is from a Gaussian centered at the experimental angular position of a plasma gun with a spot size that has increased from the initial 4.25 cm jet radius.

cell. By using $A_i = 3.5$ G cm for each component of \mathbf{A} and $\epsilon_i = 3.43\alpha_i$ G cm, the resulting initial magnetic field has a volume-averaged value of roughly 36.1 G, which, like the density, is consistent with an increase from the attained value in the 2D jet collision simulation. Furthermore, the initial volume-averaged electron Hall parameter is greater than unity and $\langle\beta\rangle$ is greater than 100, which is again consistent with the 2D jet collision simulation. The field everywhere outside of the target plasma is initialized to zero.

The Xe liner is initialized with a density of roughly 2.99×10^{-7} g cm $^{-3}$, temperature of 1.5 eV, velocity of 60 km/s, and thickness of 5 cm. For the simulation cases with liner perturbations, we imposed Gaussian density and velocity perturbations throughout the thickness of the liner at the angular positions of the experimental plasma guns. An example of this kind of perturbation is shown in Fig. 8, which displays the mathematical form (i.e., dimensionless) of the perturbation as a spherical slice at a radius of 25 cm (the inner liner radius) projected to a 2D map. The purpose of Fig. 8 is to illustrate that the regions of increased density and velocity are indeed centered at the angular positions of the experimental plasma guns, and that each Gaussian has an overall spot size larger than 4.25 cm (the initial jet radius at the chamber wall). These perturbations are normalized to have precise control of their amplitude, and we ran three simulations with 0%, 5%, and 10% perturbations.

Outside of the liner is a pseudo-vacuum, which we model as an extension of the Xe liner but with a density and velocity that decrease linearly to $2.99 \times 10^{-9} \text{ g cm}^{-3}$ and 0 km/s, respectively. The initial conditions for these simulations are summarized in Table I.

Parameter	Experimental-scale	Reactor-scale
min. cell width (cm)	0.12500	0.03125
target radius (cm)	25	4.0
target ρ (g cm^{-3})	3.35×10^{-10}	2.24×10^{-5}
target T_e, T_i (eV)	40.0	108
target $\langle B \rangle$ (G)	36.1	6.29×10^4
target $\langle \chi_e \rangle$	22.8	9.93
target $\langle \beta \rangle$	427	9.82
liner thickness (cm)	5	1
liner ρ (g cm^{-3})	2.99×10^{-7}	2.40×10^{-2}
liner T_e, T_i (eV)	1.5	1.5
liner velocity (km/s)	60	80
liner perturbations	0%, 5%, 10%	0%
vacuum ρ (g cm^{-3})	2.99×10^{-9}	2.40×10^{-6}

TABLE I. Initial conditions used for the 3D *FLASH* simulations of the experimental-scale and reactor-scale target compression.

We first look at the 0% perturbation case in detail to understand the dynamics and relevant physics. Fig. 9 shows a time series of the implosion, viewed as 2D slices of mass density (g cm^{-3}) and ion temperature (eV). At the early time of $1.6 \mu\text{s}$, the target density has more than tripled from its initial value, and a temperature gradient has been established by the competing effects of compressional heating and thermal conduction. The central temperature has increased due to compression, but the target plasma's contact with the colder liner plasma has resulted in some thermal losses. Magnetization helps reduce thermal losses to some extent, and ion temperatures overall increase. Target density and ion temperature both increase for the duration of the simulation; volume-averaged values reach 500 times the initial value and $>150 \text{ eV}$, respectively. Localized peak values may be much higher, and

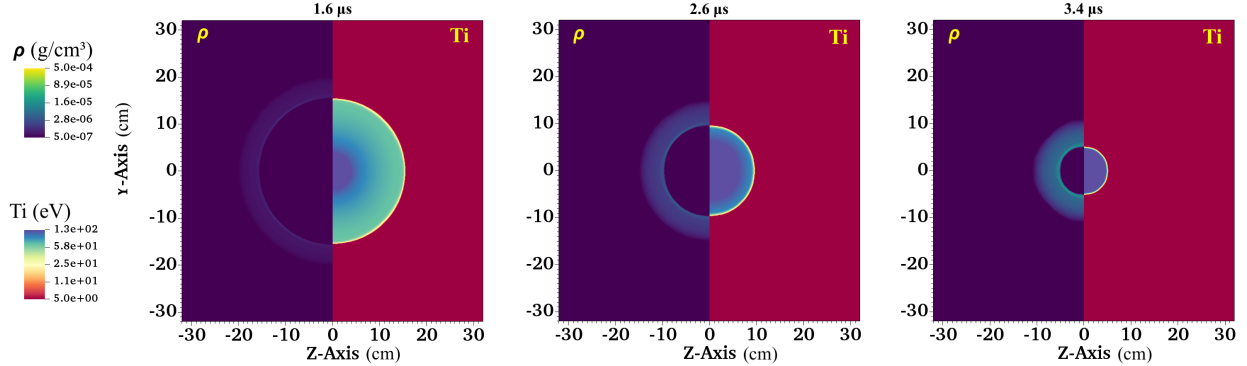


FIG. 9. A time series of slices at the y - z mid-plane showing mass density in g cm^{-3} (left halves) and ion temperature in eV (right halves) for the 0% perturbation case.

it is important to keep in mind that results could be optimized on this platform and further improved on a larger reactor-scale platform with more plasma guns. Also note that, without any liner perturbations, the implosion remains spherical.

Fig. 10 shows the same time series as the previous figure but now with magnetic field-relevant parameters: magnetic field magnitude (G), electron Hall parameter χ_e , and inverse plasma beta $1/\beta$ (the ratio of magnetic pressure to thermal pressure). There are a few key points to note here: 1) the randomization of the initial magnetic field results in peaks and valleys that make the plots appear noisy, 2) χ_e is overall less than unity as some B-field has been lost, and 3) $1/\beta$ remains very small during the simulation, i.e., the magnetic field is never dynamically important. Although χ_e has peak values >100 , these are highly localized to where the magnetic field is also peaked, thus much of the overall benefit of magnetized thermal insulation is lost. In fact, the volume-averaged χ_e inside the target drops below unity at about $0.3 \mu\text{s}$. We can see an enhancement of B-field inside the liner at $3.4 \mu\text{s}$, which suggests that the field has diffused out of the target plasma in part because the cold liner has a relatively high magnetic resistivity.

These results show that it is important for future PLX experiments to guard against magnetic field loss via resistive diffusion. In addition to simply using stronger initial fields, there are other ways this effect may be mitigated. More target preheat would decrease the target resistivity and help keep the field more “frozen-in” to the target plasma, allowing for more magnetic field compression. Keeping the liner hotter may also be beneficial, and could be achieved by using a material with a lower atomic number than Xe ($Z = 54$). A lower- Z

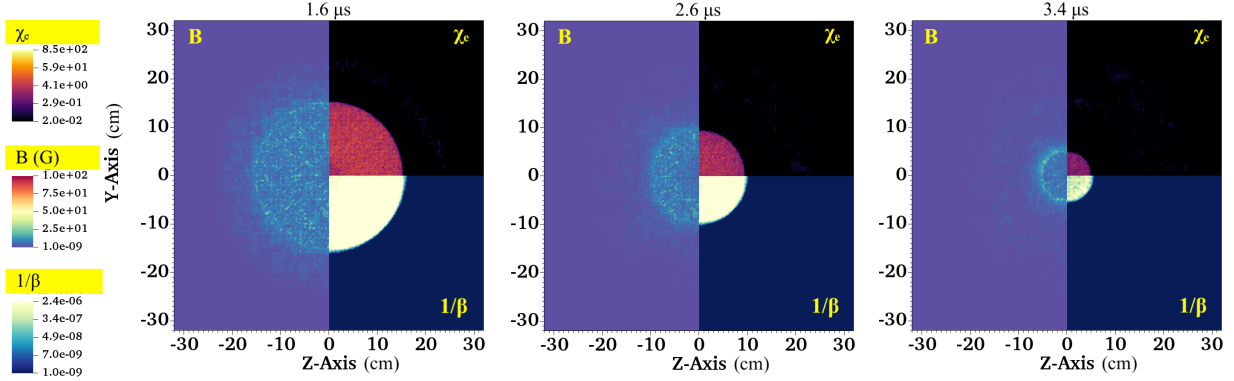


FIG. 10. A time series of slices at the y - z mid-plane showing magnetic field magnitude in G (left halves), electron Hall parameter χ_e (upper-right), and inverse plasma beta $1/\beta$ (lower-right) for the 0% perturbation case.

material would directly have a lower resistivity, but would also radiate less, keeping it hotter and thus also decreasing resistivity. Of course high- Z materials have their own benefits, namely their increased radiation losses make them colder and more effective pistons for compression. Thus there is some optimization to be done in this parameter space, but this is beyond the scope of this work.

For these experimental-scale simulations, the minimum fuel radius that can be resolved with 10 computational cells is 1.25 cm, or a convergence ratio (CR) of 20. The target plasma in the simulations may continue to compress to higher CR, but results become less reliable due to the resolution. Also, higher CRs are not expected to be attainable experimentally, so we consider $CR = 20$ to be close to stagnation. Fig. 11 shows the mass density (g cm^{-3}) and ion temperature (eV) for all perturbation cases at $4.0 \mu\text{s}$, which is when the 0% perturbation case reaches $CR = 20$. We see that the 0% case is still mostly spherical at this late time, while the perturbed cases have become distorted. In the 5% case, the target plasma is still intact, but a significant portion of it has become mixed with colder liner material resulting in final target ion temperatures 2-3x less than the 0% case. In both the 0% and 5% cases, ion temperatures before stagnation reached peak values ranging from 150-200 eV, but the target remains hotter for longer in the 0% case. The target is completely destroyed in the 10% case as liner plasma has reached the origin. Based on these results, the 5% perturbation level is a reasonable upper limit on liner non-homogeneities for maintaining a viable target plasma. The uniformity of the liner will depend on the jet merging process and physical

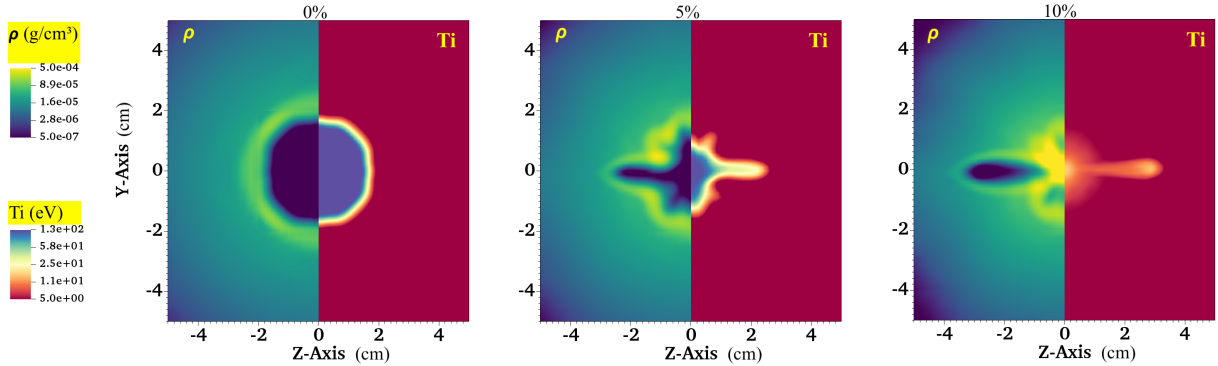


FIG. 11. 2D slices of mass density in g cm^{-3} (left halves) and ion temperature in eV (right halves) for the 0%, 5%, and 10% perturbation cases at roughly $4.0 \mu\text{s}$. This is when the 0% case reaches $\text{CR} = 20$, which is close to stagnation.

effects therein, some of which were discussed in Section IV.

Fusion will not occur under the plasma conditions attained in these experimental-scale simulations, but that was expected. The current PLX platform is primarily for testing, optimizing, and exploring relevant physics. Our target compression simulation results show the importance of liner uniformity and that ion temperatures of about 200 eV should be possible, and perhaps higher temperatures can be reached with further optimization. However, it has always been the case that PLX would need to be scaled to a larger system to be a viable option for fusion energy production, which was the impetus for the simulation presented in the next subsection.

C. Reactor-scale *FLASH* Simulation

Here we present a 3D *FLASH* target compression simulation using idealized initial conditions, which are summarized in Table I in the previous subsection. The chosen parameters represent theoretically attainable conditions for a larger, reactor-scale PLX design that employs many more plasma guns for both target and liner formation, hence the much higher densities as compared to the previous experimental-scale simulations. Furthermore, the reactor-scale simulation assumes that some perfectly-spherical compression has already taken place; the initial target radius is only 4 cm, and the initial liner thickness is 1 cm. This was done, in part, to accurately model the problem with higher resolution (a minimum cell width of 0.03125 cm) and track the compression down to smaller radii, or higher convergence

ratios. If we consider 25 cm to still be the “true” initial target radius, then this simulation is starting at $CR = 6.25$. We should also note that the target plasma in this simulation is 50/50 deuterium-tritium (DT) as opposed to pure hydrogen, and it is initialized with a higher temperature of 108 eV.

The initial magnetic field in the target is randomized with the same method as described in the previous subsection. We purposely aimed for a regime in which $\langle\chi_e\rangle$ and $\langle\beta\rangle$ were both close to 10, which is similar to the experimental-scale regime. Due to the increased density and temperature, the resulting volume-averaged field strength required to reach this regime was roughly 6.29 T.

As with the experimental-scale simulations of the previous subsection, the results of the reactor-scale simulation are reliably accurate as long as the target radius is resolved with at least 10 computational cells. This means we can resolve a minimum fuel radius of 0.3125 cm, which corresponds to an overall $CR = 80$. We consider this CR to be close to stagnation, and it is reached at roughly 320 ns. Fig. 12 shows the mass density (g cm^{-3}) and ion temperature (eV) at this time, and we observe that the target plasma has reached fusion-relevant conditions. Peak ion temperatures in the target have exceeded 1 keV, and the volume-averaged ion number density has increased by nearly a factor of 500. It is also worth noting that the implosion has remained roughly spherical to this high CR , which is perhaps not too surprising since liner perturbations were not used.

Like the experimental-scale simulations, the target plasma in the reactor-scale simulation lost some magnetic field due to resistive diffusion, but the effect was less dramatic. Despite starting with a lower electron Hall parameter, as compared to the experimental-scale case, $\langle\chi_e\rangle$ does not go below unity until about 247 ns, which corresponds to a $CR \approx 19.4$. This is much later in the compression compared to the experimental-scale 0% perturbation case, which reached this condition at a CR slightly greater than 1.0. There are multiple reasons for this including: 1) the reactor-scale liner is moving faster, giving less time for B-field to be lost, and 2) the reactor-scale target is hotter, which results in a lower magnetic resistivity. This supports the idea, presented in the previous subsection, that some magnetic field losses can be mitigated by increasing the target preheat during target formation. Using a faster liner may benefit the magnetic field, but too much interpenetration of the liner jets may not be desirable for PLX as mentioned in Section IV A.

Overall, the 3D reactor-scale simulation results are encouraging, as they show that

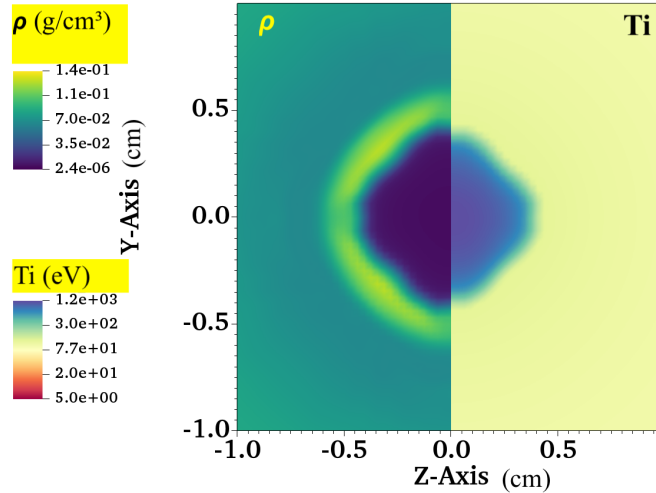


FIG. 12. A 2D slice of mass density in g cm^{-3} (left half) and ion temperature in eV (right half) for the 3D reactor-scale *FLASH* simulation at roughly 320 ns. This is when the simulation reaches $\text{CR} = 80$, which is close to stagnation. No initial liner perturbations were imposed for this simulation.

theoretically-achievable initial conditions with a larger platform can lead to fusion-relevant densities and temperatures.

VI. CONCLUSIONS

In this work, we have presented a comprehensive overview of the PLX platform using three computational codes (*FLASH*, *OSIRIS*, and *HELIOS*) to simulate the three phases of PLX: target formation, liner formation, and target compression. Each phase has its own unique set of challenges and dominant physical processes.

FLASH was used to simulate 2D target formation from two colliding magnetized plasma jets, although the actual experiment employs 4~6 jets. Jet dynamics were briefly discussed, but our primary focus was on the resulting target conditions. With jet propagation conditions within experimental ranges, the hydrogen target plasma reached peak ion temperatures of 40 eV and a volume-averaged electron Hall parameter above unity. The goal of forming a preheated, magnetized, quasi-spherical target was achieved, and we expect results to further improve when more than two target-forming jets are used.

Using both *FLASH* and *OSIRIS* in 1D, we studied the effects of initial jet velocity on the

liner formation process. The *OSIRIS* results showed that the jets were most collisional at the lowest velocity (13 km/s) and collisionless at the highest velocity (50 km/s), thus the *FLASH* results only matched well for low-velocity cases. An intermediate, quasi-collisional regime (the 25 km/s case) may be desirable, as some interpenetration of the jets led to a smooth density profile and may help mitigate hydrodynamic instabilities. We also studied the effects of radiation on liner formation using *FLASH* (*OSIRIS* does not include radiation). Results showed that with radiation on, the liner material was much colder and denser (i.e., more collisional), suggesting that *FLASH* may actually compare well to experimental results of moderate velocities (25 km/s). However, this also suggests that the velocity that results in the desirable quasi-collisional regime may be higher than 25 km/s.

We explored target compression in 1D with *FLASH*, *OSIRIS*, and *HELIOS*. All three codes showed similar implosion dynamics with peak compression near $4.5\ \mu\text{s}$ and fuel temperatures around 150 eV. Fuel temperatures in the *OSIRIS* simulation were overall slightly lower due to kinetic effects (i.e., mixing of the liner and target materials). This suggests that the MHD codes may underestimate the level of mixing depending on the relevant plasma conditions when target compression begins, but it was not an overwhelming effect.

Finally, we conducted high-fidelity 3D target compression simulations with *FLASH* to study effects of liner perturbations and determine the achievable fuel conditions. The experimental-scale simulation results were qualitatively similar to their 1D counterparts, with stagnation times near $4.0\ \mu\text{s}$ and peak ion temperatures in the 150-200 eV range. Using realistically-positioned liner perturbations, we were able to quantify the target’s tolerance to liner non-uniformities. Results point to a 5% liner perturbation level (on density and velocity) as a reasonable upper limit for maintaining a mostly spherical implosion and achieve desirable plasma conditions. An additional, idealized 3D target compression simulation highlighted what may be possible on a larger PLX system. With higher densities, a slightly higher liner velocity, and higher initial target temperature, this reactor-scale simulation reached fusion-relevant conditions with temperatures above 1 keV. All of our 3D target compression cases showed evidence of magnetic field losses due to resistive diffusion, which could potentially be mitigated in future PLX experiments.

Future experimental work on PLX will include further exploration of the parameter space to optimize initial conditions and overall performance. Our simulation results throughout this work have emphasized the key physics at play, providing guidance for that optimization

process. We have also helped make the case for a larger PLX system, which our work shows is a theoretically viable path to fusion. There is still plenty of additional simulation work that can be done, as PJMIF is such a rich concept from a physics perspective. Regardless of physics intrigue, from a fusion energy production and engineering perspective, the PLX is an attractive design and one that merits further investigation.

ACKNOWLEDGMENTS

This material is based on work supported by the U.S. Department of Energy (DOE) National Nuclear Security Administration (NNSA) under awards DE-NA0004144 and DE-NA0004147, and under subcontracts no. 630138 and C4574 with Los Alamos National Laboratory. We acknowledge support from the U.S. DOE Advanced Research Projects Agency-Energy (ARPA-E) under Award Number DE-AR0001272. This research used resources of the National Energy Research Scientific Computing Center, a DOE Office of Science User Facility supported by the Office of Science of the U.S. Department of Energy under Contract No. DE-AC02-05CH11231 using NERSC award FES-ERCAP0028680. The authors acknowledge support from the High-Performance Computing group of the Laboratory for Laser Energetics and the Center for Integrated Research Computing at the University of Rochester. The software used in this work was developed in part by the U.S. DOE NNSA- and U.S. DOE Office of Science-supported Flash Center for Computational Science at the University of Chicago and the University of Rochester. This paper describes objective technical results and analysis. Any subjective views or opinions that might be expressed in the paper do not necessarily represent the views of the U.S. DOE or the United States Government.

REFERENCES

- ¹K. Ikeda, Nuclear Fusion **47**, E01 (2007).
- ²R. Buttery, B. Covele, J. Ferron, A. Garofalo, C. Holcomb, T. Leonard, J. Park, T. Petrie, C. Petty, G. Staebler, *et al.*, Journal of Fusion Energy **38**, 72 (2019).
- ³A. Zylstra, O. Hurricane, D. Callahan, A. Kritcher, J. Ralph, H. Robey, J. Ross, C. Young, K. Baker, D. Casey, *et al.*, Nature **601**, 542 (2022).

- ⁴H. Abu-Shawareb, R. Acree, P. Adams, J. Adams, B. Addis, R. Aden, P. Adrian, B. Afeyan, M. Aggleton, L. Aghaian, *et al.*, Physical Review Letters **132**, 065102 (2024).
- ⁵S. C. Hsu, T. Awe, S. Brockington, A. Case, J. Cassibry, G. Kagan, S. Messer, M. Stanic, X. Tang, D. Welch, *et al.*, Ieee transactions on plasma science **40**, 1287 (2012).
- ⁶Y. F. Thio, S. C. Hsu, F. D. Witherspoon, E. Cruz, A. Case, S. Langendorf, K. Yates, J. Dunn, J. Cassibry, R. Samulyak, *et al.*, Fusion Science and Technology **75**, 581 (2019).
- ⁷E. C. Merritt, A. L. Moser, S. C. Hsu, C. S. Adams, J. P. Dunn, A. Miguel Holgado, and M. A. Gilmore, Physics of Plasmas **21** (2014).
- ⁸S. J. Langendorf, K. C. Yates, S. C. Hsu, C. Thoma, and M. Gilmore, Physical Review Letters **121**, 185001 (2018).
- ⁹A. L. LaJoie, F. Chu, A. E. Brown, S. J. Langendorf, J. P. Dunn, G. A. Wurden, F. Witherspoon, A. Case, M. Luna, J. Cassibry, *et al.*, Physics of Plasmas **31** (2024).
- ¹⁰K. C. Yates, S. Langendorf, S. C. Hsu, J. Dunn, S. Brockington, A. Case, E. Cruz, F. Witherspoon, Y. Thio, J. Cassibry, *et al.*, Physics of Plasmas **27** (2020).
- ¹¹A. L. LaJoie, F. Chu, S. Langendorf, J. Cassibry, A. Vyas, and M. Gilmore, Review of Scientific Instruments **94** (2023).
- ¹²D. Ryutov, Fusion science and technology **56**, 1489 (2009).
- ¹³S. C. Hsu and S. J. Langendorf, Journal of Fusion Energy **38**, 182 (2019).
- ¹⁴F. Chu, S. J. Langendorf, J. Olson, T. Byvank, D. A. Endrizzi, A. L. LaJoie, K. J. McCollam, and C. B. Forest, Physics of Plasmas **30** (2023).
- ¹⁵F. Chu, A. L. LaJoie, B. D. Keenan, L. Webster, S. J. Langendorf, and M. A. Gilmore, Physical Review Letters **130**, 145101 (2023).
- ¹⁶S. J. Langendorf and S. C. Hsu, Physics of Plasmas **24** (2017).
- ¹⁷S. C. Hsu and S. J. Langendorf, Journal of Fusion Energy **38**, 182 (2019).
- ¹⁸T. J. Awe, C. S. Adams, J. S. Davis, D. S. Hanna, S. C. Hsu, and J. T. Cassibry, Physics of Plasmas **18** (2011).
- ¹⁹J. Davis, S. Hsu, I. Golovkin, J. MacFarlane, and J. Cassibry, Physics of Plasmas **19** (2012).
- ²⁰C. Thoma, D. Welch, and S. Hsu, Physics of Plasmas **20** (2013).
- ²¹K. Schillo and J. Cassibry, Physics of Plasmas **27** (2020).
- ²²S. Thompson and J. Cassibry, Physics of Plasmas **27** (2020).
- ²³B. Fryxell, K. Olson, P. Ricker, F. X. Timmes, M. Zingale, D. Q. Lamb, P. MacNeice,

- R. Rosner, J. W. Truran, and H. Tufo, *Astrophys. J. Suppl. Ser.* **131**, 273 (2000).
- ²⁴P. Tzeferacos, M. Fatenejad, N. Flocke, C. Graziani, G. Gregori, D. Q. Lamb, D. Lee, J. Meinecke, A. Scopatz, and K. Weide, *High Energy Density Phys.* **17**, **Part A**, 24 (2015).
- ²⁵D. Lee, *J. Computat. Phys.* **243**, 269 (2013).
- ²⁶J.-Y. Ji and E. D. Held, *Phys. Plasmas* **20**, 042114 (2013), <https://doi.org/10.1063/1.4801022>.
- ²⁷P. Tzeferacos, A. Rigby, A. Bott, A. R. Bell, R. Bingham, A. Casner, F. Cattaneo, E. M. Churazov, J. Emig, N. Flocke, *et al.*, *Phys. Plasmas* **24**, 041404 (2017).
- ²⁸S. I. Braginskii, *Rev. Plasma Phys.* **1**, 205 (1965).
- ²⁹J. R. Davies, H. Wen, J.-Y. Ji, and E. D. Held, *Phys. Plasmas* **28**, 012305 (2021), <https://doi.org/10.1063/5.0023445>.
- ³⁰M. Fatenejad, B. Fryxell, J. Wöhlbier, E. Myra, D. Lamb, C. Fryer, and C. Graziani, *High Energy Density Phys.* **9**, 63 (2013).
- ³¹C. Orban, M. Fatenejad, S. Chawla, S. C. Wilks, and D. Q. Lamb, arXiv preprint arXiv:1306.1584 (2013).
- ³²C. Orban, M. Fatenejad, and D. Q. Lamb, *Physics of Plasmas* **29**, 053901 (2022), https://pubs.aip.org/aip/pop/article-pdf/doi/10.1063/5.0079493/16599359/053901_1_online.pdf.
- ³³J. P. Sauppe, Y. Lu, P. Tzeferacos, A. C. Reyes, S. Palaniyappan, K. A. Flippo, S. Li, and J. L. Kline, *Physics of Plasmas* **30**, 062707 (2023), https://pubs.aip.org/aip/pop/article-pdf/doi/10.1063/5.0144517/17992379/062707_1_5.0144517.pdf.
- ³⁴J. Meinecke, H. W. Doyle, F. Miniati, A. R. Bell, R. Bingham, R. Crowston, R. P. Drake, M. Fatenejad, M. Koenig, Y. Kuramitsu, *et al.*, *Nat. Physics* **10**, 520 (2014).
- ³⁵J. Meinecke, P. Tzeferacos, A. Bell, R. Bingham, R. Clarke, E. Churazov, R. Crowston, H. Doyle, R. P. Drake, R. Heathcote, *et al.*, *Proc. Natl. Acad. Sci. U. S. A.* **112**, 8211 (2015).
- ³⁶C. K. Li, P. Tzeferacos, D. Lamb, G. Gregori, P. A. Norreys, M. J. Rosenberg, R. K. Follett, D. H. Froula, M. Koenig, F. H. Seguin, *et al.*, *Nat. Commun.* **7**, 1 (2016).
- ³⁷P. Tzeferacos, A. Rigby, A. F. A. Bott, A. R. Bell, R. Bingham, A. Casner, F. Cattaneo, E. M. Churazov, J. Emig, F. Fiuza, *et al.*, *Nat. Commun.* **9**, 1 (2018).
- ³⁸A. Rigby, F. Cruz, B. Albertazzi, R. Bamford, A. R. Bell, J. E. Cross, F. Fraschetti,

- P. Graham, Y. Hara, P. M. Kozlowski, *et al.*, Nat. Physics **14**, 475 (2018).
- ³⁹T. G. White, M. T. Oliver, P. Mabey, M. Kühn-Kauffeldt, A. F. A. Bott, L. N. K. Döhl, A. R. Bell, R. Bingham, R. Clarke, J. Foster, *et al.*, Nat. Commun. **10**, 1 (2019).
- ⁴⁰L. E. Chen, A. F. A. Bott, P. Tzeferacos, A. Rigby, A. Bell, R. Bingham, C. Graziani, J. Katz, M. Koenig, C. K. Li, *et al.*, Astrophys. J. **892**, 114 (2020).
- ⁴¹A. F. A. Bott, P. Tzeferacos, L. Chen, C. A. J. Palmer, A. Rigby, A. R. Bell, R. Bingham, A. Birkel, C. Graziani, D. H. Froula, *et al.*, Proc. Natl. Acad. Sci. U. S. A. **118** (2021).
- ⁴²J. Meinecke, P. Tzeferacos, J. S. Ross, A. F. A. Bott, S. Feister, H.-S. Park, A. R. Bell, R. Blandford, R. L. Berger, R. Bingham, A. Casner, L. E. Chen, J. Foster, D. H. Froula, C. Goyon, D. Kalantar, M. Koenig, B. Lahmann, C. Li, Y. Lu, C. A. J. Palmer, R. D. Petrasso, H. Poole, B. Remington, B. Reville, A. Reyes, A. Rigby, D. Ryu, G. Swadling, A. Zylstra, F. Miniati, S. Sarkar, A. A. Schekochihin, D. Q. Lamb, and G. Gregori, Science Advances **8**, eabj6799 (2022), <https://www.science.org/doi/pdf/10.1126/sciadv.abj6799>.
- ⁴³R. A. Fonseca, L. O. Silva, F. S. Tsung, V. K. Decyk, W. Lu, C. Ren, W. B. Mori, S. Deng, S. Lee, T. Katsouleas, and J. C. Adam, in ... *Science—ICCS 2002*, Vol. 2331, edited by P. M. A. Sloot, A. G. Hoekstra, C. J. K. Tan, and J. J. Dongarra (Springer Berlin Heidelberg, Berlin, Heidelberg, 2002) pp. 342–351.
- ⁴⁴R. G. Hemker, F. S. Tsung, V. K. Decyk, and W. B. Mori, in *Proceedings of the 1999 Particle Accelerator Conference*, Vol. 5, edited by A. Luccio and W. MacKay (IEEE, Piscataway, NJ, 1999) pp. 3672–3674.
- ⁴⁵K. G. Miller, R. P. Lee, A. Tableman, A. Helm, R. A. Fonseca, V. K. Decyk, and W. B. Mori, Computer Physics Communications **259**, 107633 (2021).
- ⁴⁶K. Nanbu, Physical Review E **55**, 4642 (1997).
- ⁴⁷T. Takizuka and H. Abe, Journal of Computational Physics **25**, 205 (1977).
- ⁴⁸F. Peano, M. Marti, L. O. Silva, and G. Coppa, Physical Review E **79**, 025701 (2009).
- ⁴⁹F. Fiuza, M. Marti, R. A. Fonseca, L. O. Silva, J. Tonge, J. May, and W. B. Mori, Plasma Physics and Controlled Fusion **53**, 074004 (2011).
- ⁵⁰J. MacFarlane, I. Golovkin, and P. Woodruff, Journal of Quantitative Spectroscopy and Radiative Transfer **99**, 381 (2006), radiative Properties of Hot Dense Matter.
- ⁵¹E. C. Hansen, A. Frank, and P. Hartigan, The Astrophysical Journal **800**, 41 (2015).
- ⁵²S. C. Hsu, A. L. Moser, E. C. Merritt, C. S. Adams, J. P. Dunn, S. Brockington, A. Case, M. Gilmore, A. G. Lynn, S. J. Messer, and et al., Journal of Plasma Physics **81**, 345810201

(2015).

⁵³H. Wen, C. Ren, E. C. Hansen, D. Michta, Y. Zhang, S. Langendorf, and P. Tzeferacos, *Physics of Plasmas* **29**, 062706 (2022), https://pubs.aip.org/aip/pop/article-pdf/doi/10.1063/5.0087035/16622426/062706_1_online.pdf.

⁵⁴P. Cagas, J. Juno, A. Hakim, A. LaJoie, F. Chu, S. Langendorf, and B. Srinivasan, *Physics of Plasmas* **30**, 053903 (2023), https://pubs.aip.org/aip/pop/article-pdf/doi/10.1063/5.0135389/17177730/053903_1_5.0135389.pdf.

⁵⁵L. Spitzer, *Physics of Fully Ionized Gases* (Interscience Publishers, 1962).

⁵⁶J. Shang, *Journal of Computational Physics* **153**, 312 (1999).